Xu T & Cai Y. (2024) FREQUENCY-DEPENDENT EFFECTS OF ULTRASOUND-GUIDED FERROPTOSIS IN OVARIAN AND BREAST CANCER: IMPLICATIONS FOR TARGETED SONOTHERAPY, RECOVERY, AND PHYSICAL FUNCTION. Revista Internacional de Medicina y Ciencias de la Actividad Física y el Deporte vol. 24 (98.1) pp. 415-437.
DOI: https://doi.org/10.15366/rimcafd2024.98.1.028

ORIGINAL

FREQUENCY-DEPENDENT EFFECTS OF ULTRASOUND-GUIDED FERROPTOSIS IN OVARIAN AND BREAST CANCER: IMPLICATIONS FOR TARGETED SONOTHERAPY, RECOVERY, AND PHYSICAL FUNCTION

Tian Xu [1,2,*], Yijin Cai [3]

[1] School of Nursing, Wuxi Taihu University, Wuxi 214000, PR China; tianx@cwxu.edu.cn (T. X.)
[2] School of Environmental Science and Engineering, Wuxi University, Wuxi 214105, PR China;
[3] Department of general surgical, Affiliated Children's Hospital of Jiangnan University, Wuxi 214023, PR China
Email: tianx@cwxu.edu.cn

Recibido 16 de abril de 2024 **Received** April 16, 2024
Aceptado 16 de diciembre de 2024 **Accepted** December 16, 2024

ABSTRACT

Background: Low-intensity ultrasound (LIUS) is an emerging, non-invasive therapeutic strategy with potential applications in targeted cancer treatment, functional recovery, and sports medicine. However, the mechanisms underlying its frequency-dependent effects on tumor suppression remain partially understood, particularly in relation to cell-type specificity and ferroptosis induction. This study investigates the role of LIUS frequency in modulating ferroptotic pathways, focusing on its effects in ovarian (SKOV3) and breast (MDA-MB-231) cancer cells, with potential implications for minimizing systemic toxicity and preserving post-treatment physical function. **Methods:** A frequency-optimized LIUS protocol (0.3 W/cm², within acoustic safety limits) was applied to evaluate tumor suppression efficiency and ferroptosis induction. The study identified 800 kHz and 600 kHz as the most effective frequencies for ovarian and breast cancer cell inhibition, respectively, leading to enhanced ferroptotic activity. To potentiate these effects, PEG-coated magnetic iron oxide nanoparticles (Fe_3O_4@PEG) were integrated, facilitating p53-mediated ferroptotic pathways and maximizing tumor suppression. In vivo experiments were conducted to assess tumor inhibition, therapeutic safety, and the impact on systemic recovery and functional adaptation. **Results:** The combination of LIUS and Fe_3O_4@PEG nanoparticles significantly enhanced tumor suppression with minimal off-target effects, demonstrating a tumor growth

inhibition rate of up to 92%. Notably, the study confirmed that frequency-specific LIUS modulation plays a crucial role in determining cell-type selectivity and therapeutic efficacy, suggesting potential applications in precision oncology and rehabilitation medicine. **Conclusion:** This study provides strong evidence for the use of LIUS as a frequency-dependent, ferroptosis-inducing strategy for targeted cancer therapy, with minimal systemic side effects and implications for post-treatment recovery. The integration of Fe_3O_4@PEG nanoparticles enhances therapeutic precision, offering a cell-selective, minimally invasive approach to tumor suppression. Given the growing interest in non-invasive modalities that preserve physiological integrity, LIUS-based therapies may have valuable applications in sports medicine and rehabilitation, supporting oncology patients in maintaining functional mobility and optimizing post-treatment physical performance. Future research should explore the role of ultrasound-guided therapies in promoting tissue regeneration, mitigating fatigue, and improving neuromuscular recovery in cancer survivors.

KEYWORDS: Low Intensity Ultrasound; Ferroptosis; Frequency-Dependence; Nanoparticles

1. INTRODUCTION

Low-intensity ultrasound (LIUS) has emerged as a non-invasive therapeutic modality with significant potential in targeted cancer therapy, functional recovery, and rehabilitation medicine. Its mechanical and bioacoustic effects enable precise modulation of cellular activity, making it a promising tool for minimally invasive oncological interventions that preserve systemic function and physical resilience. Unlike conventional cancer therapies, which often result in widespread cytotoxicity and long-term physiological impairment, LIUS offers a cell-type-selective approach, enabling precision tumor suppression while minimizing collateral damage to healthy tissues. Among its many potential applications, LIUS has been identified as a key modulator of ferroptosis—a regulated form of cell death driven by iron-dependent lipid peroxidation, which is particularly relevant in the treatment of chemotherapy-resistant cancers such as ovarian and breast malignancies. Ovarian and breast cancers pose significant challenges in oncology and post-treatment rehabilitation, often requiring aggressive systemic therapies that contribute to chronic fatigue, metabolic dysfunction, and musculoskeletal decline. Ferroptosis, as a distinct non-apoptotic cell death pathway, has garnered attention for its unique ability to selectively target cancer cells with high metabolic activity, potentially offering a novel therapeutic alternative with fewer long-term complications. Recent studies suggest that LIUS may serve as an effective, frequency-dependent trigger for ferroptosis, offering a means to enhance cancer treatment efficacy while preserving neuromuscular function and post-treatment physical performance. However, the mechanistic effects of LIUS frequency on ferroptosis induction remain insufficiently characterized, particularly in the

context of cell-type specificity and functional recovery. To address this gap, this study investigates the selective effects of LIUS at different frequencies on ferroptosis induction in ovarian (SKOV3) and breast (MDA-MB-231) cancer cells. Utilizing a frequency-optimized LIUS protocol at 0.3 W/cm² (within acoustic safety limits), we identified 800 kHz and 600 kHz as the most effective frequencies for ovarian and breast cancer suppression, respectively, with corresponding activation of p53-mediated ferroptotic pathways. To further potentiate these effects, PEG-coated magnetic iron oxide nanoparticles (Fe_3O_4@PEG) were incorporated, leveraging their ability to enhance oxidative stress and selectively drive ferroptosis in tumor cells. In vivo validation confirmed that LIUS combined with Fe_3O_4@PEG achieved a tumor growth inhibition rate of up to 92%, with minimal systemic toxicity and preserved functional integrity (Pirmoazen et al., 2020). (Joiner et al., 2022) under acoustic energy below the cavitation threshold (Domenici et al., 2013; Louw et al., 2013). By transmission of acoustic energy through the cell membrane, cytoplasm, and nucleus, the US participates significantly in the regulation adjustment of cell behaviors and physiological processes, including migration, differentiation, proliferation, tissue repair and development (Sahu et al., 2019; Yang et al., 2023). Furthermore, Schuster et al. have established that the sensitivity of carcinoma cells to US is frequency and dose dependent (Schuster et al., 2013). At a low-level density of US (3 Ws/cm^2), human cardiac microvascular endothelial cells (hcMEC) revealed the highest proliferation effect at 510 kHz, while Madin-Darby Canine kidney epithelial cells (MDCK) at 4.36 MHz. On the contrary, mouse neuroblastoma cells (Neuro2A) exhibited a significant decrease in proliferation at 994 kHz. Significant stiffness differences are found between carcinoma cells and normal cells, leading to distinct responses of different cancer cells to different vibration frequencies, covering a frequency range of tens to hundreds of kilohertz. By adjusting the frequencies, it is thearetically feasible to implement the mechanical force of the US to selectively target tumor cells. However, questions on adopting US with selective frequencies to inhibit the biological function of carcinoma cells hasn't been solved. Ferroptosis, a programmed cell death induced by abnormal iron accumulation and lipid peroxidation (Tang et al., 2019). It could be the possibility and opportunity for cancer therapy as tumor cells display a heightened requirement for iron because of their fast proliferation. The fundamental molecular process of ferroptosis revolves around the modulation of the equilibrium between antioxidant defense and oxidative injury (Kuang et al., 2020), which is constrained by reduced glutathione (GSH), synthesis of which is limited by cysteine/glutamate transporter (system xc^-). Transmembrane transporter SLC7A11 is one of two subunits of system xc^-, SLC7A11 high overexpression in 8 different cancer cell lines were improved to suppress tumor metastasis (Yan et al., 2023). Decreasing the expression of SLC7A11/GPX4 has turned into as an available strategy for ferroptosis (Zhou et al., 2021). Tumor suppressor gene p53 (also called TP53) plays a critical role in governing

diverse cellular processes, including metabolism, aging and apoptosis. The current study on the impact of p53 and ferroptosis indicates that p53 promotes ferroptosis by downregulation of antioxidant enzymes superoxide dismutase (SOD) via the p53/SLC7A11/GPX4 (Liu & Gu, 2022). However, in specific circumstances, p53 may also impede or suppress ferroptosis. Tarangelo et al. discovered that stabilized p53 can effectively postpone the occurrence of ferroptosis in murine lung tumors (Liu & Gu, 2022). Xie et al. found a similar interaction between p53 and ferroptosis in colorectal cancer cells (Xie et al., 2017). This regulatory effect on iron-induced cell death of p53 and SLC7A11 in different types of tumors remains to be further clarified. Based on the natural demand for iron, ferroptosis was considered as an opportunity for nanomaterials in cancer therapy (Liu et al., 2023). Magnetic nanoparticles (MNPs), such as ferritic oxide nanoparticles (NPs), have been extensively utilized in the field of biomedicine owing to their favorable biocompatibility, superparamagnetic characteristics, and hyperthermic effects (Song et al., 2015). Therapeutic applications encompass tumor magnetic hyperthermia, magnetic drug targeting, and magnetic transfection, while diagnostic uses include magnetic resonance imaging. Appropriately modified MNPs demonstrate good biocompatibility, with commonly used modifying molecules including polyethylene glycol (PEG) (Song et al., 2015), dextran (Wang et al., 2021), phospholipids (Dhiman et al., 2022), and 2,3-DMSA (Sen et al., 2021). PEG is an FDA-approved synthetic polymer for in vivo injection, and the modified MNPs not only exhibit good biocompatibility but also possess outstanding anti-protein adsorption capabilities, thereby extending their circulation time in the blood (Song et al., 2015). We answer these questions by exploring the variations in the sensitivity and cellular response of different tumor cells to ultrasonic frequencies under extremely low acoustic energies below the cavitation threshold, as well as the mechanism underlying this acoustic anti-tumor effects of mechanical force combined with Fe_3O_4 NPs in vitro and in vivo. Ultimately, improving tumor suppression efficiency and reducing unexpected drug allergies or tissue injuries (Cui et al., 2023).

2. Materials and Methods

2.1. Cell Lines

Human epithelial ovarian carcinoma cell line SKOV3 (TChu185) and human breast carcinoma cell line MDA-MB-231 (TCHu227) were purchased from Cell Bank of the Chinese Academy of Sciences (Shanghai, China).

2.2. Animals

BALB/c nude mice (female, aged 6-8 weeks, 19-21 g) were purchased from Beijing Vital River Laboratory Animal Technology Co., Ltd (Beijing, China). The animal study protocol was approved by the Animal Care and Use

Committee of Southeast University, China (protocol code #20200407003).

2.3. Low Intensity Ultrasound (LIUS) Treatment Protocols

This research content was segmented into four sections. First of all, Section I was to investigate the anti-tumor effects of different acoustic frequency for SKOV3 cells and MDA-MB-231 cells. Then ultrasonic parameters should be optimized according to tumor suppression indicators. Section II was to explore ferroptosis in frequency-dependent LIUS therapy (optimized parameters obtained from Section I) with Fe_3O_4 NPs (Ploussard, 2017). The anti-tumor mechanism of frequency-dependent LIUS combined with Fe_3O_4 NPs was demonstrated in Section III. Ultimately, in vivo trails, ferroptosis and apoptosis performances were estimated in Section IV. The protocols of ultrasonic radiation were as follows: Section I: once the cells are seeded, the deaerated water was poured in the ultrasonic chamber until the immersion of the upper fixation plate. The probe emitted ultrasonic waves at an angle of 15 ° below the 12-well culture plate. At different frequencies (20 kHz, 600 kHz, 800 kHz, 1 MHz) under the intensity of 0.3 W/cm^2, the transducer of the ultrasonic device was clung to the cell-culture plate, and each well was irradiated for 20 s, 40 s, or 60 s. Section II and Section III: optimized ultrasonic parameters were applied to cells as described in Section I. The optimized ultrasonic parameters were 800 kHz for SKOV3 cells and 600 kHz for MDA-MB-231 cells at 0.3 W/cm^2 for 20 s. Section IV: To prevent overheating by long term acoustic radiation, a water barrier was applied on the ultrasonic probe. Medical ultrasound coupling agent was applied on the surface of the tumor. Additionally, continuous monitoring of the nude mice's condition and the tumor surface damage was conducted during the ultrasound radiation process. In the groups of LIUS and LIUS combined with Fe_3O_4 NPs, ultrasonic radiations were performed on the tumor site for 3×10^8 cycle/day in 2 weeks (Louw et al., 2013).

2.4. Section I: Anti-Tumor Effects of Frequency-Dependent Ultrasonic Radiation

2.4.1. Detection of the Relative Proliferation Rate by MTT Assay

At each time point after ultrasonic radiation (12, 24, 36 and 48 h), 100 μL of MTT solution (5 mg/mL) was added to each well separately. Then the plate was incubated in CO_2 incubator at 37 °C for 4h. Subsequently, discarding the medium and adding 750 μL dimethyl sulfoxide (DMSO) to each well before the optical density (OD) value was read by ELISA at 570 nm wavelength. The relative proliferation rate:

$$\text{relative proliferation rate} = \frac{OD_e - OD_b}{OD_c - OD_b} \times 100\% \quad (1)$$

where OD_e is the value of the experimental group, OD_b is the value of

the blank group, OD_c is the value of the control group.

2.4.2. Intracellular Reactive Oxygen Species Assay and Cell Apoptosis Analysis

24 hours after ultrasonic treatment, digested cells were collected. Then the detections were conducted for ROS (S0033), GSH (S0053), SOD (S0101) and malondialdehyde (MDA, S0131) tests, following the instructions from Beyotime, and cell apoptosis analysis were followed from Nanjing KeyGEN Biotech (China, KGA108-1). Membrane fluidity and cytoskeleton were detected to reflect o xidative damage to membrane structure (Supplementary Materials S1.1-1.2).

2.4.3. Cell Invasiveness and Migration Capability Analysis

24 hours after the ultrasonic treatment, the cells were collected and plated at 10^5/well to the transwell insert coated with prepared Matrigel (354230, BD, USA). The medium was supplemented with 150 μL, and 600 μL RPMI-1640 medium containing 50 % FBS was added to the chamber. After incubating the plate for 24 h, the insert was carefully removed from the plate, and the medium in the insert was discarded (An et al., 2023; Coudray et al., 2017; Krasovitski et al., 2011; Tang et al., 2017). Then the insert was stained with 0.1 % crystal violet solution for 30 min, followed by washing with PBS for a couple seconds. Once the membrane was air dried, the insert was observed after placing it under 200 x bio-intelligent navigator and counting. Cell migration capability analysis was followed with supplementary material S1.3.

2.5. Section II: Ferroptosis in Frequency-Dependent LIUS Therapy with or without Fe_3O_4 NPs

2.5.1. Synthesis and Characterization of Fe_3O_4@PEG

Synthesis of the Fe_3O_4@DMSA particles were followed by Zou et al. (Zou et al., 2014), then mixed Fe_3O_4@DMSA particles with a 0.1 mM HS-PEG solution (0.05 M phosphate buffer solution, pH 8) by sonication for 30 s, the resulting material, PEG-modified Fe_3O_4 (Fe_3O_4@PEG), was stored in water. The morphology and structure of Fe_3O_4@PEG were observed by transmission electron microscopy (TEM, Hitachi, Japan). 2 mL of the magnetic NPs diluted in PBS buffer solution (pH 7.4) was loaded into a cuvette for measurement of particle size and zeta potential on a Zeta-Sizer Nanoserie at 90° scattering angle (Malvern, British). The imaging capacity of magnetic NPs was detected by MRI (HT-MRSI65-35A, Hua Tong Nuclear Magnetic, China).

2.5.2. Verification of Ferroptosis

Each type of cells was incubated at a density of 105 until the cell density

reached about 85 %, then divided into 5 groups: control group, LIUS group, LIUS + Fer-1(inhibitor of ferroptosis) group, LIUS + Fe_3O_4@PEG group and LIUS + Fe_3O_4@PEG + Fer-1 group. Each well contained 5×10^3 cells. Before acoustic radiation, LIUS + Fer-1 and LIUS + Fe + Fer-1 (2 M) groups were replaced by fresh culture medium with ferroptosis inhibitor Fer-1 (2 M), while other groups with nothing. LIUS protocol was described above. The relative cell viability of each group was detected by MTT assay 24h after acoustic radiation.

2.5.3. Detection of Intracellular Lipoperoxide and GPX4

Cells were incubated and divided into 5 groups as above. The culture medium was then discarded, and the wells were rinsed with PBS twice. Subsequently, for intracellular lipoperoxide analysis, 500 µL of C-11 BODIPY dye solution (5 M) was added to each well and incubated in the dark at 37 °C for 30 minutes. The dye solution was then removed, and the wells were rinsed three times with PBS before analysis by flow cytometry or imaging by confocal laser scanning microscopy. Meanwhile, analysis of GPX4 was followed the instruction form Enzyme Linked Biotechnology (Beijing, China).

2.6. Section III: Anti-Tumor Mechanism of Frequency-Dependent LIUS Combined with Fe_3O_4 NPs

2.6.1. Western Blot Assay

To determine the expression levels of the ferroptotic proteins of GPX4 and SCL7A11(ab125066, ab175186, Abcam, USA), as well as the apoptosis-related proteins of p53 and c-CAS3 (ab26, ab32042, Abcam, USA), SKOV3 and MDA-MB-231 cells were plated into six-well plates at a density of 10^6 under the condition mentioned above. Then, fresh media containing PBS (control), nothing (LIUS), Fe_3O_4@PEG (Fe) and Fe_3O_4@PEG (LIUS + Fe) were replaced in before acoustic radiation. Both LIUS and LIUS + Fe groups were treated by ultrasound as did in Section II.

Total proteins were harvested by cell lysis using Laemmli Sample Buffer (Bio-Rad) and quantified by electrophoresis using 10% SDS-polyacrylamide gel electrophoresis and a BCA protein kit (Sigma-Aldrich). Subsequently, the protein was transferred to a polyvinylidene difluoride (PVDF) membrane (Millipore, Bedford, USA) and sequentially blocked by the primary and secondary antibodies. Finally, the images were captured on automatic chemiluminescence imaging analysis Tanon 5200 system (Inner Mongolia Ketong, China). To explore the timeline of cell death, both c-CAS3 and PGX4 were tested in the first 12 h after sonication (0, 1, 2, 3, 4, 5, 6, 8, 10, 12 h). Furthermore, p53, apoptosis and ferroptosis inhibitors were applied to investigate their influence on cell death programs in LIUS combined with ferritic NPs.

2.7. Section IV: Ferroptosis and Apoptosis Performances in vivo

2.7.1. Construction of Xenograft-Bearing Nude Mice

Each BALB/c nude mouse was injected under the skin (near the fore limb) with 5 x 106 cells of each cell type suspended in 100 μL PBS, and the volume of the tumor reached 70 mm3 (calculated in the following equation), indicating successful tumor construction and ready for the subsequent experiments:

$$\text{tumor volume } (mm^3) = A \times B^2/2 \quad (2)$$

Where "A" and "B" stand representing the tumor's longest and shortest diameters, respectively.

2.7.2. Treatment Procedures

Mice were divided into four groups, and the treatment procedures was in the table below. Volume of tumor and mice's weight had measured each other day in the two-week treatment.

Ultrasonic radiation was operated 6 h after injection of ferritic NPs, and MR exam was applied 6 h after that. At the end of the treatment, mice were sacrificed, and the tissue of tumors were collected for western blot assay and Immunohistochemistry (IHC).

Table 1: Groups and a Two-Week Treatment Procedure In Vivo (N = 4)

GROUPS	ULTRASONIC TREATMENT	DOSE OF FERRITIC NPS	TREATMENT FREQUENCY
CONTROL	-	-	Injection with 200 μL saline solution via caudal vein once a week
LIUS	0.3 W/cm^2, 800 kHz, 8 min 30 s for ovarian cancer model; 0.3 W/cm^2, 600 kHz, 8 min 30 s for breast cancer model	-	Once a day
Fe_3O_4@PEG	-	5 mg/kg in 200 μL saline solution	Injection with ferritic NPs via caudal vein once a week
LIUS + Fe_3O_4@PEG	0.3 W/cm^2, 600 kHz, 8 min 30 s for ovarian cancer model; 0.3 W/cm^2, 800 kHz, 8 min 30 s for breast cancer model	5 mg/kg in 200 μL saline solution	LIUS radiation once a day; injection with ferritic NPs via caudal vein once a week

2.7.3. MR Examination

MR images were obtained using a magnetic resonance scanner with a T2 flash sequence. All mice were then injected via the tail vein at a dosage of 5 mg Fe per kg body weight. Three mice were included in this study. In vivo signal reception was conducted using a 3.8 cm circular surface coil. The imaging parameters were as follows: field of view (FOV) = 100 mm^2, TRTE = 408 ms, 3.5 ms, matrix size = 256256, and slice thickness = 1 mm (Song et al., 2015).

2.7.4. Histological Distribution Study

Soak the tumor tissue in a 4% neutral formalin solution for 24 hours to fix it, then encase it in paraffin blocks. Employ a rotary microtome to cut the tissue blocks into slices approximately 6 μm. Levels of apoptosis in tumor tissue were determined by TUNEL (TdT-mediated dUTP Nick-End Labeling) stain, and so did ferritic ions by Prussian blue and nuclear fast red double staining.

2.7.5. Immunohistochemical (IHC) Staining

According to the standard protocol, we performed immunohistochemical assays for carcinoma samples. Serial sections were deparaffinized, blocked with 3% (wt/vol) bovine serum albumin (BSA), and then incubated overnight with anti-SLC7A11, anti-GPX4, anti-p53 and anti-c-CAS3. Subsequently, the sections were incubated with a secondary antibody including anti-mouse or anti-rabbit for 1 h.

2.8. Statistical Analysis

All the statistical analyses were carried out using IBM SPSS 20.0 (IBM, Armonk, NY, USA). Continuous variables were reported as the mean (± standard deviation) and categorical variables reported as n (%). The statistical inference and comparative analysis of continuous data were performed by Student's t-test or one-way ANOVA with LSD test. Comparison of data at different time points was analyzed by One-way repeated measure ANOVA. Each experiment in vitro was repeated independently at least three times.

3. Results

3.1 Section I: Anti-Tumor Effects of Frequency-Dependent LIUS Radiation

3.1.1 The Ultrasonic Inhibition on the Proliferation of Carcinoma Cells

The ultrasonic inhibition on the proliferation of cancer cells was frequency dependent ($p < 0.0001$, Figure 1a). The lowest relative proliferation rate of MDA-MB-231 cells was at 600 kHz for 20 s (32.32 %), while that of SKOV3 cells at 800 kHz for 40 s (20.23 %). Both carcinoma cells reflected no

response on 20 kHz radiation. We could not detect significant statistical differences between observation time points (p = 0.241), for the convenience of subsequent experimental detections, the observation time was set at 24 h after 20 s LIUS treatment.

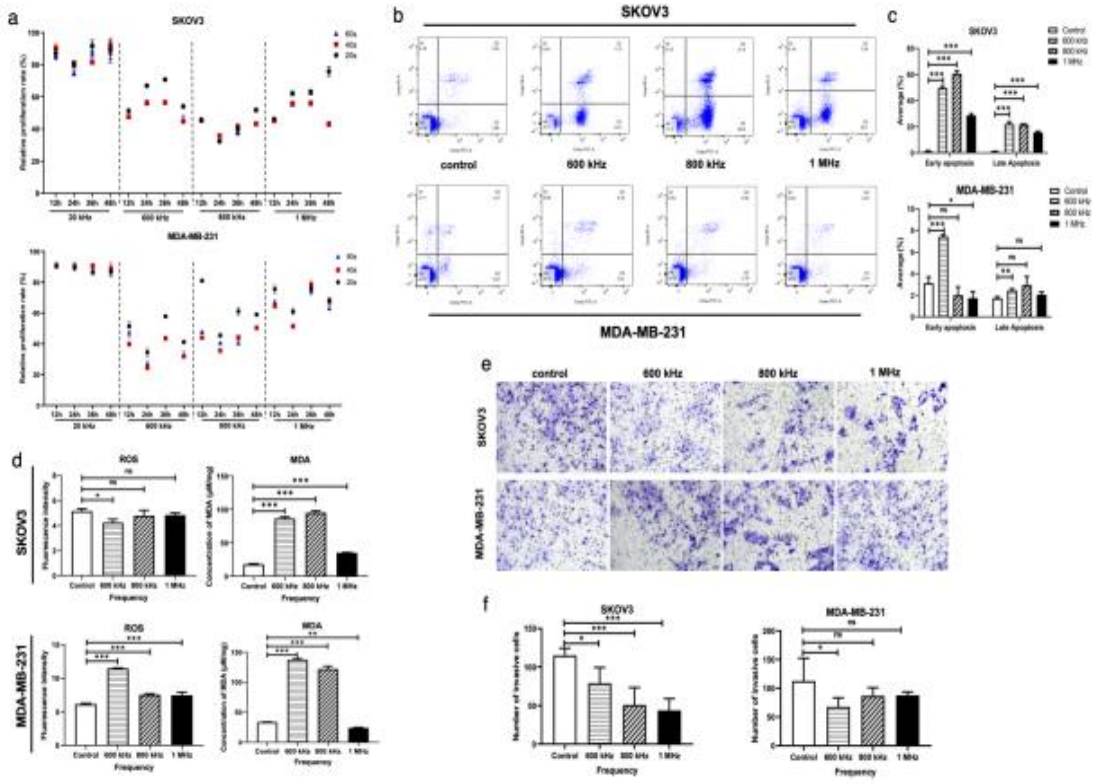

Figure 1: Anti-Tumor Effects of LIUS radiation in different frequencies. (a) Effects of US on the relative proliferation rate of SKOV3 and MDA-MB-231 cells for 20 s, 40 s and 60 s radiation at 20, 600, 800 kHz and 1 MHz in 48 h; (b,c) Cell apoptosis at 600, 800 kHz and 1 MHz, 0.3 W/cm^2, 20 s; (d) Effects of different ultrasonic frequencies on the ROS and MDA levels of carcinoma cells (* presented p <0.05, ** presented p <0.01, *** presented p <0.001); Cell invasiveness analysis (e,f) at different ultrasonic frequencies (* presented p<0.05, *** presented p <0.001).

3.1.2 The Effects of Different Ultrasonic Frequencies on Cell Functions

Next, we found a frequency-dependent apoptosis process in both cell lines (Figure 1b, c). After 600 kHz radiation on MDA-MB-231 cells, the rates of early and late apoptosis increased to 2.37 times and 1.42 times respectively compared to the untreated group (p < 0.0001 and p = 0.005, respectively). A similar trend of SKOV3 cells was observed at 800 kHz, the rates of early and late apoptosis increased to 59.88 times and 21.80 times respectively compared to the untreated cells (p < 0.0001). The cell capability of invasion (Figure 1e,f) and migration (Figure S1) decreased significantly from the baseline. Especially in cell invasion test, the number of membranes permeating for SKOV3 cells reached the lowest point at 800 kHz (p = 0.007), for MDA-MB-231 cells was the

lowest at 600 kHz ($p = 0.0403$).

3.1.3 The Effects of Different Ultrasonic Frequencies on Oxidative Stress

The intracellular oxidative stress levels of carcinoma cells were further evaluated, and that of SKOV3 cells reached the peak at 800 kHz frequency (Figure 1d, S2). The MDA level was 5.81 folds more than that of the control ($p < 0.0001$, Figure 1d), with SOD and GSH levels decreasing to 46.88 % and 84.62 %, respectively ($p < 0.0001$, Figure S2). Equivalently, the ROS level of MDA-MB-231 cells was 1.21-fold more than that of the control cells at 600 kHz ($p < 0.0001$), while the MDA level was 4.08-fold higher ($p < 0.0001$, Figure 1d). SOD and GSH levels decreased to 12.99 % and 67.46 %, compared to the control group ($p < 0.0001$, Figure S2). From this observation, we concluded that the US played a significant role in modulating the oxidative stress, including lipid peroxidation, at optimized frequency. Intracellular oxidative damage leads to impaired lipid peroxides of membrane and membrane lipid fluidity, which is one of the characters of ferroptosis (Stockwell, 2018). Therefore, the experiments of membrane lipid fluidity illustrated that impaired lipid peroxides of membrane occurred after LIUS irradiation. Both cell lines presented the lowest membrane lipid fluidities of 3.61 and 4.34 at 800 kHz and 600 kHz, respectively (Figure S3). And significant changes in the monofilament structure were observed in immunofluorescence results (Figure S4). Considering the above results comprehensively, 800 kHz and 600 kHz (both at 0.3 W/cm^2 for 20 s) were optimized for exploring the LIUS death mode for SKOV3 and MDA-MB-231 cells in the subsequent Section II-III.

3.2 Section II: Ferroptosis in Frequency-Dependent LIUS Therapy with Fe3O4 NPs

Another character of ferroptosis is the exhaustion of intracellular GSH and decreased GPX4 activity. Based on the results of high MDA levels and decreased GSH levels after ultrasonic treatment in both cell types, we hypothesized that ferroptosis might occurred in the process. Ferroptosis inhibitor, ferrostatin-1 (fer-1), was applied to verify the hypothesis by reversing this oxidative damage, while ferritic NP was synthetized not only as a ferroptosis inducer to verify reversely, but also a diagnostic and therapeutic dual-purpose substance (An et al., 2023).

3.2.1 Characterization of the Fe_3O_4 NPs

The core material was the Fe_3O_4@DMSA magnetic NPs, which showed a narrow size distribution, (15.6 ± 1.5) nm, as confirmed by TEM in Figure 2a and c. After being coated with PEG, the core diameter of Fe_3O_4@PEG remained consistent at (18.2 ± 1.8) nm, and the NPs were observed well dispersed and encased in a phospholipid PEG membrane (Figure 2b). Superparamagnetic NPs agented with hydrodynamic size at (44.2 ± 0.74) nm

(Figure 3d), the zeta potential of the samples was averaging −16.7 mV (Figure S5).

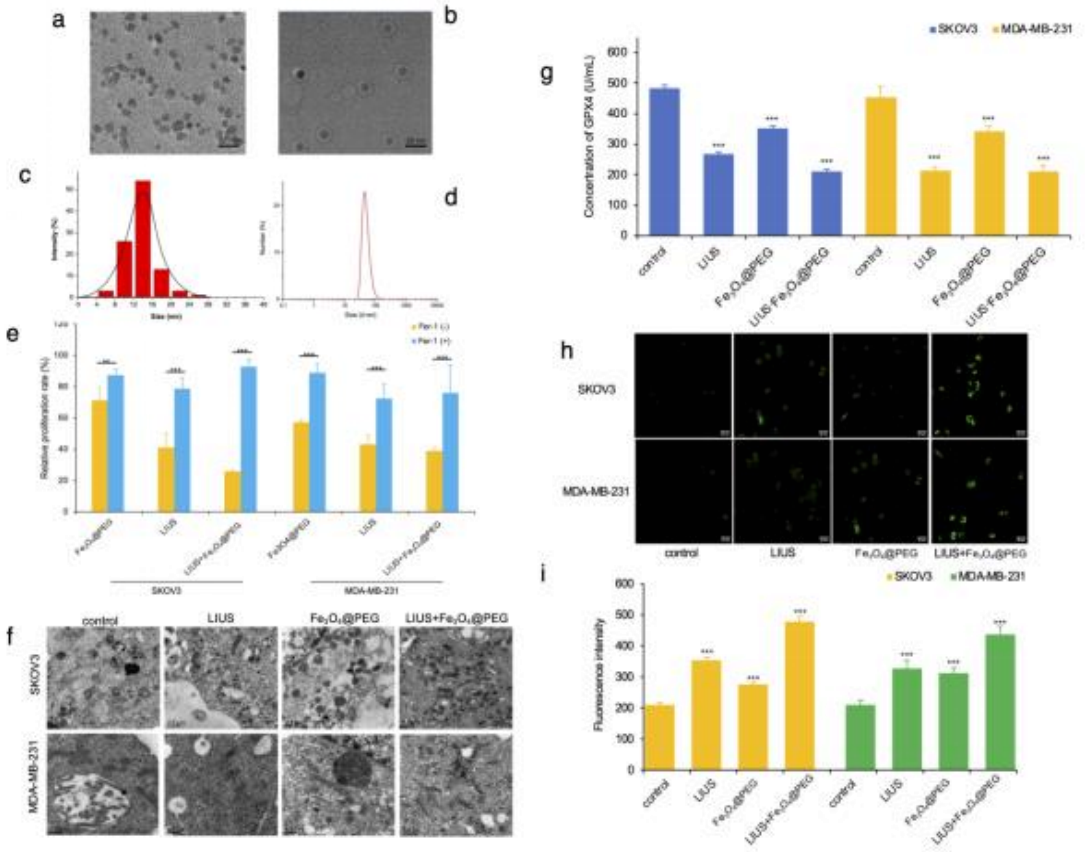

Figure 2: Ferroptosis in Frequency-Fependent LIUS Therapy with Fe_3O_4 NPs. TEM Images of Fe_3O_4@DMSA (a) and Fe_3O_4@PEG (b), bar = 20 nm; Particle size distribution (c), hydrodynamic size (d) of Fe_3O_4@PEG; (e) Ferroptosis inhibitor, Fer-1, revised cell death in LIUS treated cells; (f) The morphological changes of carcinoma cells were depicted by TEM, bar = 0.5 μm; (g) Concentration of cellular GPX4 was analyzed by ELISA; (h,i) Lipid-ROS was detected by C11 BODIPY fluorescent probe, bar = 20 μm (*** presented p <0.001).

Next, we evaluated the magnetic properties of the MNPs. Fe_3O_4@PEG exhibited a Ms of 70 emug, along with zero coercivity and remanence, indicating its superparamagnetic properties (Figure S6a). It was observed that as the Fe concentration increased, the brightness of the solution decreased significantly, as shown in Figure S6c. Furthermore, Fe_3O_4@PEG at 1.5T magnetic resonance was calculated to be 135.05 mM-1s-1(Figure S6b). This value is comparable to that of clinically available contrast agents Resovisit (approximately 70 $mM^{-1}s^{-1}$) and Feridex (120 $mM^{-1}s^{-1}$), suggesting that the synthesized nanoprobes satisfy the requirements for in vivo studies.

3.2.2 Fer-1 Revised Cell Death in LIUS Treated Cells

Then we firstly verified ferroptosis by applying the ferroptosis inhibitor in

three treatment groups for both cell lines, showed in Figure 2e. 24 h after the addition of inhibitors, fer-1 could reverse cell death in all treatment groups ($p < 0.0001$), suggesting that ferroptosis occurred with the independent or combined use of LIUS and Fe_3O_4@PEG. However, there was a distinction between SKOV3 cells and MDA-MB-231 cells, as LIUS + Fe_3O_4@PEG induced maximum cell death (relative proliferation rate 26.02 %) in SKOV3 cells ($p < 0.0001$), while no significant difference was examined in cytotoxicity between LIUS (43.25 %) and LIUS + Fe_3O_4@PEG (39.23 %) groups were observed in MDA-MB-231 cells.

3.2.3 Detection of Ferroptosis

After the interesting findings above, we evaluated the characters of ferroptosis by analyzing the intrasellar lipid peroxidation and the expression of GPX4. Most important of all, the TEM test was the golden standard for ferroptosis, validating by shrinking mitochondria and increased double membrane density of mitochondria, especially in LIUS treated and LIUS + Fe_3O_4@PEG treated cells (Figure 2f). Ferroptosis was associated with the depletion of intracellular GPXs, with GPX4 being the most prominent. Subsequent analysis indicated that the LIUS + Fe_3O_4@PEG group exhibited the lowest levels of intracellular GPX4 in both cell lines (both $p < 0.0001$, Figure 2g). Similar to the results in the cell death in different treatment groups, there was no difference in intracellular GPX4 between the LIUS group and LIUS + Fe_3O_4@PEG group ($p = 0.807$). Finally, fluorescent staining of lipid peroxidation using C-11 BODIPY (Figure 2h,i) revealed significantly higher levels in the LIUS + Fe_3O_4@PEG group compared to the Fe_3O_4@PEG group in two types of cancer cells (both $p < 0.0001$). Above all, our results indicated that frequency-dependent LIUS therapy had a potent synergistic impact on enhancing the susceptibility to ferroptosis in the presence of adequate iron.

3.3 Section III: Anti-Tumor Mechanism of Frequency-Dependent LIUS Combined with Fe3O4 NPs

3.3.1 Timeline of Expression of Key Proteins of Ferroptosis and Apoptosis

The expression of c-CAS3 in SKOV3 cells reached maximum levels at 4 h after LIUS combined with Fe_3O_4 NPs treatment and remained elevated since that. Similar findings were observed in MDA-MB-231 cells at 8 h post-treatment (Figure 3a-c). Meanwhile, SKOV3 and MDA-MB-231 cells attained the lowest GPX4 expression level at 2 h and 3 h after combined treatment, respectively, maintaining a decreased level compared to the untreated group. This indicated that ferroptosis occurred early in the damage caused by the combined treatment, preceding the onset of apoptosis.

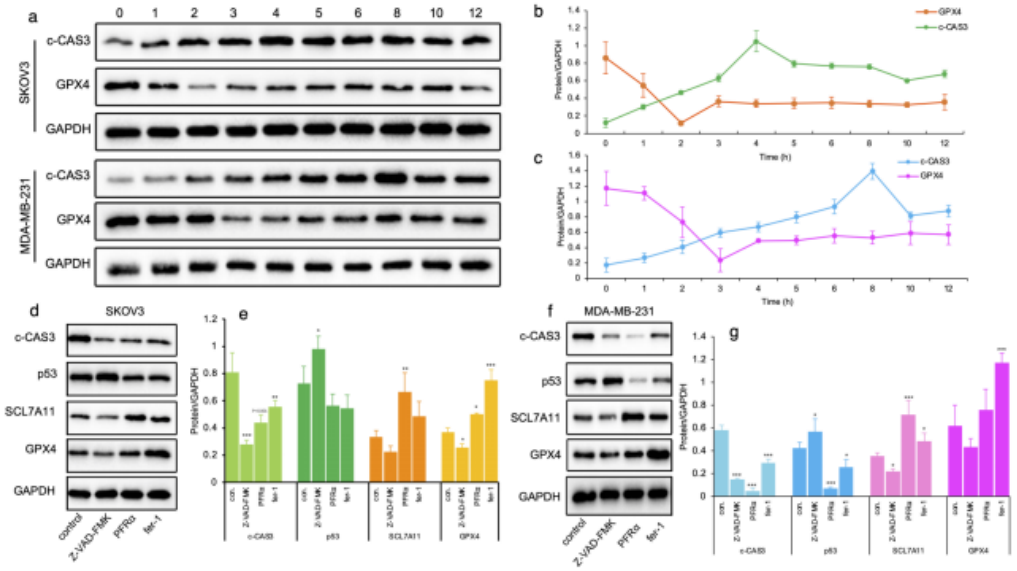

Figure 3: Expression of Key Proteins of Ferroptosis and Apoptosis After Treatment of LIUS with/without Fe_3O_4@PEG. (a-c) c-CAS3 and GPX4 expression levels in SKOV3 and MDA-MB-231 cells within 12 h after LIUS combined with Fe_3O_4 NPs; Effect of Z-VAD-FMK, PFR α and Fer‐1 on the expression of c-CAS3, p53, SCL7A11 and GPX4 in SKOV3 (d,e) and MDA-MB-231 (f,g) cells. (* presented $p < 0.05$, ** presented $p < 0.01$, *** presented $p < 0.001$)

3.3.2 Inhibition Application on Ferroptosis and Apoptosis

Then we utilized inhibitors of apoptosis, p53 and ferroptosis to investigate the interplay between the observed two programmed cell deaths, apoptosis and ferroptosis, following treatment with LIUS- Fe_3O_4@PEG treatment (Figure 3d-g). Initially, the apoptosis inhibitor (Z-VAD-FMK) led to a decreased expression level of GPX4 in SKOV3 cells ($p = 0.046$) and SCL7A11 in MDA-MB-231 cells ($p = 0.029$), while simultaneously increasing the expression of p53 in both SKOV3 and MDA-MB-231 cells ($p = 0.028$ and $p = 0.023$ respectively). These findings suggested that suppressing apoptosis did not affect the process of ferroptosis, nor did the suppression of p53. As described above, p53 assumes an essential role in regulating both apoptosis and ferroptosis. The WB results further demonstrated that the downregulation of c-CAS3 was observed in both SKOV3 and MDA-MB-231 cells after the application of the p53 inhibitor, PFR α ($p = 0.001$ and $p < 0.0001$, respectively). Conversely, SCL7A11 expression level was upregulated in both cancer cells ($p = 0.005$ and $p < 0.0001$, respectively), and GPX4 was upregulated in SKOV3 cells ($p = 0.027$), indicating that p53 promoted cell apoptosis and ferroptosis in both carcinoma cells, particularly in SKOV3 cells. Ultimately, inhibition of ferroptosis by fer-1 led to decreased expression of c-CAS3 in SKOV3 cells ($p = 0.048$) and decreased expression of c-CAS3 and p53 in MDA-MB-231 cells ($p < 0.001$ and $p = 0.011$, respectively). The GPX4 expression level increased by 2.02-fold in SKOV3 cells ($p < 0.0001$) and 1.88-fold in MDA-MB-231 cells (p

< 0.0001) than that of the corresponding control group, while the SCL7A11 expression level increased by 37.90 % in MDA-MB-231 cells (p = 0.031). Our findings confirmed inhibition of cellular ferroptosis was effective in reducing cell apoptosis.

3.4 Section IV: Ferroptosis and Apoptosis Performances in vivo

3.4.1 Tumor Inhibition by LIUS Combined with Fe3O4 NPs in Xenograft-Bearing Nude Mice

To investigate this anti-tumor effect in vivo, a subcutaneous xenograft model was established in nude mice by subcutaneously injecting ovarian cancer cells and breast cancer cells with or without injection of ferritic NPs. Throughout the 2-week treatment, no deaths were recorded among the nude mice. The tumor volume in each group decreased compared to the control group ($p < 0.0001$, Figure 4a and b). The most significant reduction rate was observed in the LIUS+ Fe_3O_4@PEG group at 91.99 % for ovarian tumor, and for breast tumor, it was 92.44 % in the LIUS group, and followed by the LIUS + Fe_3O_4@PEG group at 87.18 %.

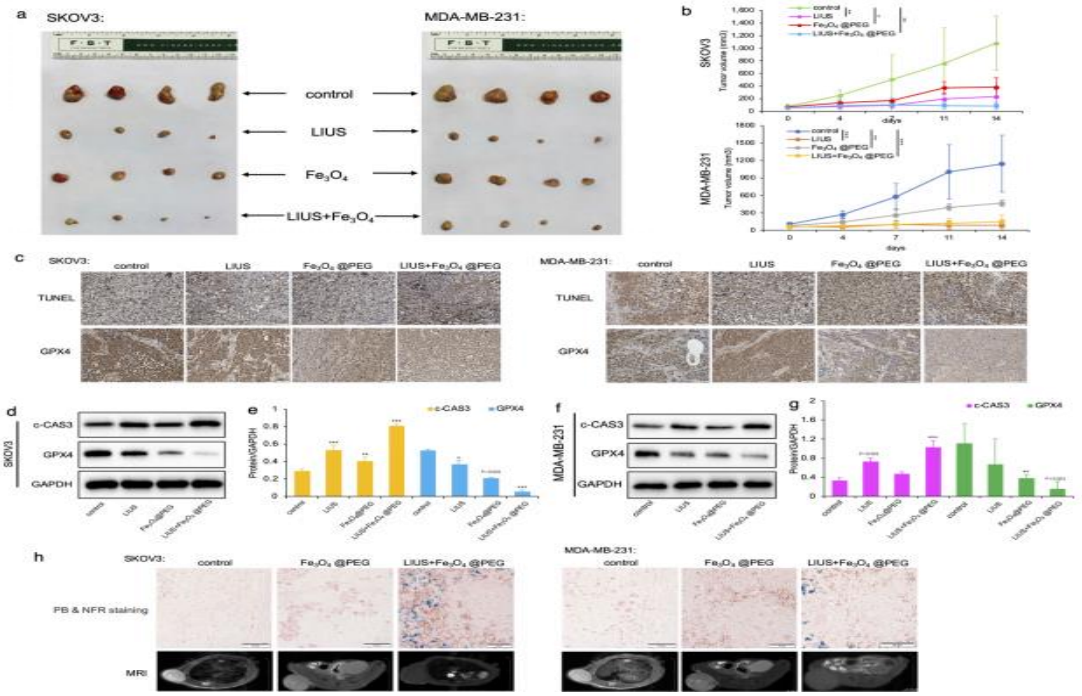

Figure 4: Therapeutic Efficacy of LIUS-Fe_3O_4@PEG treatment in vivo. (a) Subcutaneous xenograft tumors derived from SKOV3 and MDA-MB-231 cells in nude mice (n = 4/group); (b) Tumor volume variation during the 2-week therapeutic period (* $p < 0.05$, ** $p < 0.01$, *** $p < 0.001$); (c) TUNEL and IHC of GPX4 of xenograft tumor tissue; Expression of c-CAS3 and GPX4 in SKOV3 cell xenografts (d,e) and MDA-MB-231 cell xenografts(f,g), scale bar: 50 μm (* presented $p < 0.05$, ** presented $p < 0.01$, *** presented $p < 0.001$); (h) MRI T2 images and ex vivo PB & NFR staining images of tumor-bearing BABL/c mice by LIUS-Fe_3O_4@PEG (5 mg Fe/kg body weight) treatment.

3.4.2 IHC Results

After TUNEL staining, apoptotic cells showed a brownish-yellow color in the nucleus. Immunohistochemistry (Figure 4c) revealed TUNEL-positive staining across all treatment groups, featuring typical features of apoptosis such as condensed chromatin. The LIUS combined with Fe_3O_4@PEG group showed a significantly higher number of TUNEL-positive cells for both cancer cells, while the content of GPX4 was lowest. Consequently, it can be concluded that apoptosis and ferroptosis were prevalent in tumor tissues with LIUS-magnetic nanoprobe treatment.

3.4.3 WB Assay

Consist with the findings of TUNEL, apoptosis was observed in all treatment groups based on the WB analysis of c-CAS3. The LIUS + Fe_3O_4@PEG group exhibited significantly higher c-CAS3 expression levels in both types of tumors ($p < 0.0001$). In addition, this combined treatment resulted in decreased GPX4 expression compared to the control group ($p < 0.0001$, Figure 4d-g). Combined with the results of IHC, it was speculated that the LIUS + Fe_3O_4@PEG group inhibited the growth of ovarian cancer and breast cancer solid tumors by mechanisms involving not only apoptosis but also ferroptosis.

3.4.4 MR examination and PB & NFR Staining

To evaluate the application of the Fe_3O_4@PEG nanomicelles as a negative contrast agent in cancer imaging, tumor MRI images were conducted 12 hours after treatment (Figure 4h). The MR signals of the tumor sites in the magnetic NPs group and LIUS + magnetic NPs groups were lower than those the control, which did not receive an injection of iron oxide magnetic nanoprobes. With LIUS guidance, the MR signal was lower than that of the group receiving only magnetic nanoprobes, indicating that magnetic nanoprobes can initially target tumor tissues. Subsequently, cells can uptake more magnetic nanoprobes, which was validated by the PB & NFR staining. The results illustrated that a limited number of blue particles were present within the tumor mass in Fe_3O_4 group, and the combined treatment group presented the greatest quantity of blue particles.

4. Discussion

In the present study, the anti-tumor effects of ultrasonic frequencies on the relative proliferation rate of two cancer cell lines were investigated utilizing a multifactorial approach. Results from our study revealed that the ultrasonic inhibition of the proliferation rate of cancer cells is frequency dependent. We found that the inhibition in the relative proliferation rate of MDA-MB-231 cells was lowest at 600 kHz (Coudray et al., 2017; Tang et al., 2017). The inhibition

of the proliferation rate of SKOV3 cells was found to be at the lowest at 800 kHz. In our previous work, little or no cavitation was involved under the same ultrasonic radiation. The bioeffects emerged by LIUS below the cavitation threshold due to the mechanical force of US (Xu et al., 2020). Mechanical streaming on the cell membranes, triggers the signal which transmits through the cytoplasm and cytoskeleton, and ultimately reaches to the nucleus (Louw et al., 2013). Cells with strong metabolism, including carcinoma cells, have higher membrane fluidity than normal cells, making it accessible for material exchange acceleration, proliferation, epithelial mesenchymal transformation and potential invasiveness (Mehrabi et al., 2023). Thus, recent studies adopt appropriate drugs to reduce the membrane fluidity of carcinoma cells, so as to inhibit the proliferation and metabolism (Bompard et al., 2020; Mehrabi et al., 2023). Our study also demonstrated that ultrasonic treatment influenced the membrane lipid fluidity in both the SKOV3 and MDA-MB-231 cells, whereas the control cells were not impacted. Alteration in membrane fluidity not only a sign of early cell damage, but also an indication of a rigid membrane, which further enhances the sensitivity of cancer cells to US (Foglietta et al., 2021; Wang et al., 2011). Previous studies have established that mechanical force arising from the US is capable of regulating the oxidative stress, life cycle, apoptosis, proliferation, adhesiveness, migration, mitosis and other variant biological processes of cancer cells (Tang et al., 2015). Furthermore, the cytoskeleton rearrangement of cancer cells can be observed by adopting fluorescence-labeled phalloidin to stain microfilament F-actin.

Mizrahi and her colleagues' work revealed the weakest fluorescence signal after ultrasonic treatment at sensitive frequencies, with blurred microfilament structure along the radiation distribution of cell growth, which represents an accelerated disaggregation of cytoskeleton at sensitive frequencies. On the other hand, they also found that applying low-power ultrasonic irradiation on human airway smooth muscle cells resulted in the disaggregation and rearrangement of the cytoskeleton (Mizrahi et al., 2012). In addition, Samandari et al. conducted model simulation inference and cell experiments in an acoustic field of 150 ~ 250 kPa (0.8 ~ 1.7 MHz, 10 ~ 30 s), and their report demonstrated that the ultrasonic response of the nucleus is weaker than that of cytoskeleton (Samandari et al., 2017). Ultrasound (40 kHz, 1 W/cm^2, 5min) disrupted the microtubule cytoskeleton of Ovarian cancer cells (OVCAR4) and had a small effect on cell killing (35 %), but no major impact on MDA-MB-231 cells (Cui et al., 2023). Thus, this study suggested that cell membranes and cytoskeleton are more sensitive to US, and they are likely to be the main sites of action of the frequency-dependent biological effects. In our study, the most significant indicator of oxidative stress level, MDA, increased 5.81 times and 4.08 times respectively in both the SKOV3 and MDA-MB-231 cells. In another study, Jia et al. found an increased level of lipid oxidation for

breast cancer cells MCF-7 with rising ultrasonic power. With the rising of ultrasonic power to 3 W/cm^2, the MDA level significantly elevated when compared to the control group (Wang et al., 2011). We speculate that the frequency variation is reflected in the significant difference in lipid peroxidation levels at the same low ultrasonic power (around 0.3 W/cm^2). Meanwhile, the accumulation of lipid peroxidation exacerbates the loss of the lipid bilayer of cell membrane. Moreover, when the complete oxidation of regional phospholipids happens, the formation of holes will decrease the fluidity and integrity of cells. Moreover, the elevated oxidative stress level resulted in the disaggregation of cytoskeleton, thus enhancing the anti-tumor efficacy of the US. The microfilament fracture and F-actin reticular structural failure is both a typical characteristic of apoptosis, and a key event to trigger apoptosis. Furthermore, the US at sensitive frequencies significantly accelerated apoptosis in cancer cells in our study, especially in SKOV3 cells. When comparing to the control group, the rate of early apoptosis increased to 59.88 times, and the rate of late apoptosis also elevated 21.80 times ($p < 0.0001$). Meanwhile, for MDA-MB-231 cells, the rate of early apoptosis was 2.37 times that of the control group ($p < 0.0001$), and the rate of late apoptosis was 1.42 times that of the control group ($p = 0.005$).

Besides, US can alter the distribution of cell cycles. The invasiveness and migration capabilities of both carcinoma cell lines decreased after ultrasonic radiation ($p < 0.0001$). In a study, Wei et al. (2014) found that the decrease in invasiveness and migration capabilities of prostatic cancer cells after ultrasonic treatment (21 kHz, 46 mW/cm^2, 30 s), which corroborates our findings. The above study also suggested that the US had influence on the apoptosis of cancer cells, and apoptosis is another important biological process for decreasing invasiveness and migration capabilities. In addition, the recombination and extension of microfilaments provide power for cell movement and migratory transfer, and microfilament decomposition of cytoskeleton under ultrasonic stimulation blocks the precondition for cancer cell movement. On one hand, based on the findings that elevated levels of intracellular ROS after the US radiation not only caused cell apoptosis, but also provided conditions for occurring ferroptosis. On the other hand, LIUS assisted the uptake of ferritic ions. The fluorescence signal of C-11 BODIPY labeled intracellular ferritic ion after LIUS radiation was higher than that of untreated cells and was enhanced by adding Fe_3O_4@PEG into the culture medium. Both Zhou's team and ours' validated that both apoptosis and ferroptosis occurred in sonodynamic anti-tumor nanotherapy. Chen and his colleagues constructed a nanosonosensitizer (PpIX)-based liposomal NPs to assist sonodynamic cancer treatment. But there was no evidence in this research to exclude sonication with the 1 min-acoustic radiation at 1.0 MHz, 1.0 W·cm^{-2}, 50 % duty cycle. To avoid possible hazards to surrounding healthy cells, the ultrasonic energy applied in

our experiments was 0.3 $W \cdot cm^{-2}$ with TIS (MI) of 5 (1.43), which was below the current safety requirement defined by the American Federal Drugs Administration (FDA) in 2023, where MI < 1.9. The biosafety of LIUS used in this study under-cavitation threshold was provided in our previous work, without arising transient cavitation (Xu et al., 2020). Within the GPXs family, GPX4 is a crucial subunit, with GSH serving as its primary reducing substrate. Reduced GSH levels will hinder GPXs activity, consequently reducing cellular uptake of Cys and GSH synthesis, inhibiting GPX4 activity, and increasing cell susceptibility to ferroptosis through the suppression of SLC7A11 expression. By using inhibitors to suppress cell apoptosis, changes in the expression level of SCL7A11 in SKOV3 cells and GPX4 in MDA-MB-231 cells in response to LIUS combined with ferritic NPs were not observed. Meanwhile, the GPX4 expression level in SKOV3 cells and the SCL7A11 expression level in MDA-MB-231 cells were slightly down-regulated (29.73 % and 37.14 %, respectively). On the contrary, PFR α, the inhibitor of p53, induced decreased SCL7A11 and GPX4 expression in two carcinoma cells. Further investigation by Jiang and Kon's team revealed that p53 heightened the susceptibility of carcinoma cells to ferroptosis by suppressing the activation of SLC7A11 (Wang & Zhao, 2025), thereby establishing SLC7A11 as a novel functional target of the p53 gene. We also found the inhibition of ferroptosis by Fer-1 suppressed the expression of c-CAS3, and ferroptosis occurred 2 h and 5 h before apoptosis in ovarian cancer and breast cancer cells, respectively. Consequently, it can be reasonably deduced that ferroptosis accelerated cell apoptosis in both ovarian cancer and breast cancer by this combination therapy. Recent research confirmed that the US enabled to improve ferroptosis sensitivity, thus achieving synergistic apoptosis. The inhibition of tumor growth by LIUS combined with ferritic NPs was then validated in animal experiments, as well as ferroptosis and apoptosis. The Prussian blue staining results indicated a potential link between increased uptake of iron oxide NPs and the occurrence of ferroptosis in vivo. The efficacy of the iron oxide nano-probe in targeting tumors was assessed through MRI scans at the tumor site. As a paramagnetic material, the magnetic nano-probe can reduce the relaxation time of nearby protons, thus serving as an effective positive contrast agent for MR imaging and contributing to diagnostic purposes. Moreover, injuries were observed in the relatively high-dose groups (20 and 40 mg/kg of Fe_3O_4-nanoparticles) for daily injection in 1 week, and 5 mg/kg was recommended as the safety dose. In our study, the dose was 7-fold lower than that (once a week at a dose of 5 mg/kg), which was guaranteed by ultrasonic mechanical force-induced membrane permeability at the irradiation area.

5. Conclusions

Different carcinoma cells demonstrated significant frequency dependency on LIUS. Under LIUS treatment within the sensitive frequency

range, the morphological changes, and cellular changes such as, the oxidative stress level and related biological activities were most evident. Ferroptosis participated in the cell death mechanism initiated by LIUS, occurring earlier than apoptosis. The tumor-suppressing impact of LIUS was enhanced by extra magnetic Fe_3O_4@PEG. This process not only elevated apoptosis levels through p53 activation but also intensified iron-induced cell death. LIUS enabled even a small amount of nano-iron to achieve high tumor inhibition in vivo applications, ensuring both safety and the promotion of this combined diagnostic and therapeutic approach.

Funding

This research was funded by Young Scientists Fund in National Natural Science Foundation of China (82101339); General Program of Natural Science Foundation of Jiangsu Province (BK20221205); General Program of Natural Science Research of Jiangsu Higher Education Institutions of China (20KJB320034) and Universities' Philosophy and Social Science Research in Jiangsu Province (2022SJYB0988).

Institutional Review Board Statement

The animal study protocol was approved by the Animal Care and Use Committee of Southeast University, China (protocol code #20200407003 and April 7th 2020 of approval).

Acknowledgments

We wish to thank Meng Tang (Southeast University) for his advice for NPs design.

REFERENCES

An, J., Hong, H., Won, M., Rha, H., Ding, Q., Kang, N., Kang, H., & Kim, J. S. (2023). Mechanical stimuli-driven cancer therapeutics. *Chemical Society Reviews*, *52*(1), 30-46.

Bompard, J., Rosso, A., Brizuela, L., Mebarek, S., Blum, L. J., Trunfio-Sfarghiu, A.-M., Lollo, G., Granjon, T., Girard-Egrot, A., & Maniti, O. (2020). Membrane fluidity as a new means to selectively target cancer cells with fusogenic lipid carriers. *Langmuir*, *36*(19), 5134-5144.

Coudray, S., Fabre, C., Aichoun, I., & Perez-Martin, A. (2017). Anaphylactic shock with an ultrasound contrast agent. *JMV-Journal de Médecine Vasculaire*, *42*(6), 384-387.

Cui, H., Sun, Y., Zhao, D., Zhang, X., Kong, H., Hu, N., Wang, P., Zuo, X., Fan, W., & Yao, Y. (2023). Radiogenomic analysis of prediction HER2 status in breast cancer by linking ultrasound radiomic feature module with

biological functions. *Journal of Translational Medicine*, *21*(1), 44.

Dhiman, N., Sarvaiya, J., & Mohindroo, P. (2022). A drift on liposomes to proliposomes: Recent advances and promising approaches. *Journal of Liposome Research*, *32*(4), 317-331.

Domenici, F., Giliberti, C., Bedini, A., Palomba, R., Luongo, F., Sennato, S., Olmati, C., Pozzi, D., Morrone, S., & Congiu Castellano, A. (2013). Ultrasound well below the intensity threshold of cavitation can promote efficient uptake of small drug model molecules in fibroblast cells. *Drug Delivery*, *20*(7), 285-295.

Foglietta, F., Pinnelli, V., Giuntini, F., Barbero, N., Panzanelli, P., Durando, G., Terreno, E., Serpe, L., & Canaparo, R. (2021). Sonodynamic treatment induces selective killing of cancer cells in an in vitro co-culture model. *Cancers*, *13*(15), 3852.

Joiner, J. B., Kren, N. P., Durham, P. G., McRee, A. J., Dayton, P. A., & Pylayeva-Gupta, Y. (2022). Low-intensity focused ultrasound produces immune response in pancreatic cancer. *Ultrasound in Medicine & Biology*, *48*(11), 2344-2353.

Krasovitski, B., Frenkel, V., Shoham, S., & Kimmel, E. (2011). Intramembrane cavitation as a unifying mechanism for ultrasound-induced bioeffects. *Proceedings of the National Academy of Sciences*, *108*(8), 3258-3263.

Kuang, F., Liu, J., Tang, D., & Kang, R. (2020). Oxidative damage and antioxidant defense in ferroptosis. *Frontiers in cell and developmental biology*, *8*, 586578.

Liu, Q., Zhao, Y., Zhou, H., & Chen, C. (2023). Ferroptosis: challenges and opportunities for nanomaterials in cancer therapy. *Regenerative Biomaterials*, *10*, rbad004.

Liu, Y., & Gu, W. (2022). p53 in ferroptosis regulation: the new weapon for the old guardian. *Cell Death & Differentiation*, *29*(5), 895-910.

Louw, T. M., Budhiraja, G., Viljoen, H. J., & Subramanian, A. (2013). Mechanotransduction of ultrasound is frequency dependent below the cavitation threshold. *Ultrasound in Medicine & Biology*, *39*(7), 1303-1319.

Mehrabi, S. F., Elmi, S., & Nylandsted, J. (2023). Repurposing phenothiazines for cancer therapy: compromising membrane integrity in cancer cells. *Frontiers in Oncology*, *13*, 1320621.

Mizrahi, N., Zhou, E. H., Lenormand, G., Krishnan, R., Weihs, D., Butler, J. P., Weitz, D. A., Fredberg, J. J., & Kimmel, E. (2012). Low intensity ultrasound perturbs cytoskeleton dynamics. *Soft matter*, *8*(8), 2438-2443.

Pirmoazen, A. M., Khurana, A., El Kaffas, A., & Kamaya, A. (2020). Quantitative ultrasound approaches for diagnosis and monitoring hepatic steatosis in nonalcoholic fatty liver disease. *Theranostics*, *10*(9), 4277.

Ploussard, G. (2017). Re: Salvage High-intensity Focused Ultrasound (HIFU) for Locally Recurrent Prostate Cancer After Failed Radiation Therapy: Multi-institutional Analysis of 418 Patients. *European Urology*, *73*(1), 140-141.

Sahu, N., Miller, A., Viljoen, H. J., & Subramanian, A. (2019). Continuous low-intensity ultrasound promotes native-to-native cartilage integration. *Tissue Engineering Part A*, *25*(21-22), 1538-1549.

Samandari, M., Abrinia, K., Mokhtari-Dizaji, M., & Tamayol, A. (2017). Ultrasound induced strain cytoskeleton rearrangement: An experimental and simulation study. *Journal of Biomechanics*, *60*, 39-47.

Schuster, A., Schwab, T., Bischof, M., Klotz, M., Lemor, R., Degel, C., & Schäfer, K.-H. (2013). Cell specific ultrasound effects are dose and frequency dependent. *Annals of Anatomy-Anatomischer Anzeiger*, *195*(1), 57-67.

Sen, R., Ganguly, S., Ganguly, S., Debnath, M. C., Chakraborty, S., Mukherjee, B., & Chattopadhyay, D. (2021). Apigenin-loaded PLGA-DMSA nanoparticles: a novel strategy to treat melanoma lung metastasis. *Molecular Pharmaceutics*, *18*(5), 1920-1938.

Song, L., Zang, F., Song, M., Chen, G., & Zhang, Y. (2015). Effective PEGylation of Fe3O4 nanomicelles for in vivo MR imaging. *Journal of nanoscience and nanotechnology*, *15*(6), 4111-4118.

Stockwell, B. R. (2018). Ferroptosis: Death by lipid peroxidation. *Free Radical Biology and Medicine*, *120*, S7.

Tang, C., Fang, K., Guo, Y., Li, R., Fan, X., Chen, P., Chen, Z., Liu, Q., & Zou, Y. (2017). Safety of sulfur hexafluoride microbubbles in sonography of abdominal and superficial organs: retrospective analysis of 30,222 cases. *Journal of Ultrasound in Medicine*, *36*(3), 531-538.

Tang, D., Kang, R., Berghe, T. V., Vandenabeele, P., & Kroemer, G. (2019). The molecular machinery of regulated cell death. *Cell research*, *29*(5), 347-364.

Tang, J., Guha, C., & Tomé, W. A. (2015). Biological effects induced by non-thermal ultrasound and implications for cancer therapy: a review of the current literature. *Technology in cancer research & treatment*, *14*(2), 221-235.

Wang, L., & Zhao, X. (2025). ANALYSE OF PHYSICAL EXERCISE SHORT VIDEO PRODUCTION AND TRANSMISSION MECHANISM BASED ON BIG DATA ANALYSIS. *Revista multidisciplinar de las Ciencias del Deporte*, *25*(99), 59-74.

Wang, S., Fontana, F., Shahbazi, M.-A., & Santos, H. A. (2021). Acetalated dextran based nano-and microparticles: synthesis, fabrication, and therapeutic applications. *Chemical Communications*, *57*(35), 4212-4229.

Wang, X., Wang, Y., Wang, P., Cheng, X., & Liu, Q. (2011). Sonodynamically induced anti-tumor effect with protoporphyrin IX on hepatoma-22 solid tumor. *Ultrasonics*, *51*(5), 539-546.

Xie, Y., Zhu, S., Song, X., Sun, X., Fan, Y., Liu, J., Zhong, M., Yuan, H., Zhang, L., & Billiar, T. R. (2017). The tumor suppressor p53 limits ferroptosis by blocking DPP4 activity. *Cell reports*, *20*(7), 1692-1704.

Xu, T., Lu, X., Peng, D., Wang, G., Chen, C., Liu, W., Wu, W., & Mason, T. J. (2020). Ultrasonic stimulation of the brain to enhance the release of

dopamine–A potential novel treatment for Parkinson's disease. *Ultrasonics Sonochemistry*, *63*, 104955.

Yan, Y., Teng, H., Hang, Q., Kondiparthi, L., Lei, G., Horbath, A., Liu, X., Mao, C., Wu, S., & Zhuang, L. (2023). SLC7A11 expression level dictates differential responses to oxidative stress in cancer cells. *Nature communications*, *14*(1), 3673.

Yang, Y., Du, M., Yu, J., & Chen, Z. (2023). Biomechanical Response of Cancer Stem Cells to Low-intensity Ultrasound. *Journal of Biomechanical Engineering*, *145*(9), 091001.

Zhou, X., Zou, L., Chen, W., Yang, T., Luo, J., Wu, K., Shu, F., Tan, X., Yang, Y., & Cen, S. (2021). Flubendazole, FDA-approved anthelmintic, elicits valid antitumor effects by targeting P53 and promoting ferroptosis in castration-resistant prostate cancer. *Pharmacological research*, *164*, 105305.

Zou, J., Peng, Y.-G., & Tang, Y.-Y. (2014). A facile bi-phase synthesis of Fe 3 O 4@ SiO 2 core–shell nanoparticles with tunable film thicknesses. *Rsc Advances*, *4*(19), 9693-9700.